Journal of Rock Mechanics and Geotechnical Engineering 14 (2022) 407–422

Contents lists available at ScienceDirect

Journal of Rock Mechanics and Geotechnical Engineering

journal homepage: www.jrmge.cn

Full Length Article

Characterization of 3D pore nanostructure and stress-dependent permeability of organic-rich shales in northern Guizhou Depression, China

Xiaofang Jiang [a,b], Shouchun Deng [a,b,*], Haibo Li [a,b], Hong Zuo [a,b]

[a] State Key Laboratory of Geomechanics and Geotechnical Engineering, Institute of Rock and Soil Mechanics, Chinese Academy of Sciences, Wuhan, 430071, China
[b] University of Chinese Academy of Sciences, Beijing, 100049, China

ARTICLE INFO

Article history:
Received 7 May 2021
Received in revised form
14 July 2021
Accepted 20 August 2021
Available online 21 December 2021

Keywords:
Focused ion beam scanning electron microscopy (FIB-SEM)
Three-dimensional (3D) reconstruction
Pulse decay permeability (PDP)
Stress sensitivity
Wufeng–Longmaxi formation

ABSTRACT

The three-dimensional (3D) pore structures and permeability of shale are critical for forecasting gas production capacity and guiding pressure differential control in practical reservoir extraction. However, few investigations have analyzed the effects of microscopic organic matter (OM) morphology and 3D pore nanostructures on the stress sensitivity, which are precisely the most unique and controlling factors of reservoir quality in shales. In this study, ultra-high nanoscale-resolution imaging experiments, i.e. focused ion beam-scanning electron microscopy (FIB-SEMs), were conducted on two organic-rich shale samples from Longmaxi and Wufeng Formations in northern Guizhou Depression, China. Pore morphology, porosity of 3D pore nanostructures, pore size distribution, and connectivity of the six selected regions of interest (including clump-shaped OMs, interstitial OMs, framboidal pyrite, and microfractures) were qualitatively and quantitatively characterized. Pulse decay permeability (PDP) measurement was used to investigate the variation patterns of stress-dependent permeability and stress sensitivity of shales under different confining pressures and pore pressures, and the results were then used to calculate the Biot coefficients for the two shale formations. The results showed that the samples have high OM porosity and 85% of the OM pores have the radius of less than 40 nm. The OM morphology and pore structure characteristics of the Longmaxi and Wufeng Formations were distinctly different. In particular, the OM in the Wufeng Formation samples developed some OM pores with radius larger than 500 nm, which significantly improved the connectivity. The macroscopic permeability strongly depends on the permeability of OM pores. The stress sensitivity of permeability of Wufeng Formation was significantly lower than that of Longmaxi Formation, due to the differences in OM morphology and pore structures. The Biot coefficients of 0.729 and 0.697 were obtained for the Longmaxi and Wufeng Formations, respectively.

1. Introduction

Globally, the Upper Ordovician–Lower Silurian organic-rich shales are widely distributed and are a set of high-quality marine shales (Lüning et al., 2000). In China, these marine shales are known as the Upper Ordovician Wufeng Formation and Lower Silurian Longmaxi Formation, and are mainly distributed in the basin margins of the middle and upper part of the Yangtze Platform, similar to the conditions in North America (Guo, 2013). In particular, the Wufeng–Longmaxi marine shales in the south of the Sichuan Basin have good conditions for organic matter (OM) development, i.e. high gas content and suitable burial depth (Huang et al., 2012; Xin et al., 2019). In this region, several shale gas fields with commercial value have been built successively (He et al., 2018). The northern Guizhou is structurally part of the northern Guizhou–Wuling Depression beyond the southern margin of the Sichuan Basin, China. Based on previous studies on the tectonic background, organic-rich shale thickness, organic geochemical characteristics, and OM preservation, it is considered to be suitable to carry out the geological research of shale gas reservoirs in northern Guizhou, China (Yan, 2017). In particular, Xishui County,

* Corresponding author. State Key Laboratory of Geomechanics and Geotechnical Engineering, Institute of Rock and Soil Mechanics, Chinese Academy of Sciences, Wuhan, 430071, China.
E-mail address: scdeng@whrsm.ac.cn (S. Deng).

Peer review under responsibility of Institute of Rock and Soil Mechanics, Chinese Academy of Sciences.

https://doi.org/10.1016/j.jrmge.2021.08.019

located in the northern Guizhou Depression tectonics, has been extensively developed for the Upper Ordovician Wufeng Formation–Lower Silurian Longmaxi Formation shale reservoir. However, the pore structures and physical properties, such as porosity and permeability of shale reservoirs, have not been well studied.

Compared with conventional oil and gas reservoirs, the complex pore nanostructures in shale reservoirs is the bottleneck of long-term sustainable exploitation of shale gas (Yang et al., 2017). Fluids of different phases flow through or are adsorbed in the pores between or inside the organic or mineral particles (Ji et al., 2012), including nanoscale organic pores and pores between the pyrite particles, microscale and nanoscale mineral pores, and micro-fractures (Saraji and Piri, 2015; Ji et al., 2019a). Some of these pores are isolated from each other, while some are interconnected and form a pore network with natural or artificial fractures. In order to further understand the mechanism of oil and gas storages and migrations in shale, many researchers have numerically investigate fluid flow and transport in these complex pore networks (Mehmani et al., 2013; Tahmasebi et al., 2016; Xia et al., 2020). Therefore, three-dimensional (3D) characterizations of pore nanostructures (especially connected nanoscale pore networks) as well as OM and mineral components are essential for understanding the production performance of shale reservoirs.

Currently, the best method for 3D characterization as well as quantitative and qualitative analysis of shale pore nanostructure through direct visualization is focused ion beam-scanning electron microscopy (FIB-SEM) with imaging resolution up to several nanometers per voxel. The FIB-SEM employs a dual-beam system, in which the gallium ion beam mills the sample surface to a specified thickness and the electron beam continuously images the milled surface. With the help of 3D reconstruction algorithms, the contiguous milling and sequential imaging of two-dimensional (2D) image datasets can thus visualize the 3D structures of OM, minerals, organic pores, and inorganic pores or fractures. The obtained 3D image dataset can be further used for fluid flow simulation and multiscale 3D digital core reconstructions. Goral et al. (2019a) segmented images of the organic-rich region of Vaca Muerta shale scanned by FIB-SEM at an ultra-high resolution of 2.5 nm × 2.5 nm × 5 nm (length × width × height) through machine learning. They then reconstructed the 3D pore structure and quantitatively analyzed the organic pore size distribution and the effective porosity. Zhang et al. (2019) studied the relationship between the element size and pore connectivity by analyzing 600 consecutive high-resolution SEM images of the Eagle Ford shale sample, and obtained the size of representative elementary volume (REV) describing the pore connectivity. Goral et al. (2020a) used GeoDict software (Linden et al., 2018) to simulate the single-phase fluid flow with the 3D pore structural model reconstructed from FIB-SEM images. They compared changes in porosity and permeability under different stresses. Numerous scholars are keen to combine different imaging methods at different scales, such as FIB-SEM, nano-CT, micro-CT, and industrial CT, to reconstruct 3D digital cores for characterization of multiscale pore structures (Ma et al., 2019; Goral et al., 2019b, 2020b; Ji et al., 2019a, b).

In addition to pore structure characterization, the stress-dependent permeability and effective stress of the shale matrix have critical implications for predicting shale gas production capacity and gas well production. Shale reservoirs with high stress sensitivity have a rapid decrease in permeability at the beginning of extraction, which significantly reduces gas production and affects the stable production. Therefore, understanding the stress sensitivity and actual effective stress of shale reservoirs can help guide the differential control of production pressure and reduce production damages during the extraction. Haghi et al. (2020) adopted an innovative technique to measure the continuous change of porosity and absolute permeability in Berea Sandstone under various isotropic isothermal effective confining pressures. They derived semi-empirical equations to analyze the stress-dependent porosity and absolute permeability. Haghi et al. (2021) proposed a novel coupling approach to quantify poromechanical impacts on fluid-fluid displacement in porous media by coupling conceptual proxy modeling and pore network modeling techniques to reconstruct pore-deformation of water-wet Indiana limestone and simulate multiphase flow within the deformed pore space. Unfortunately, all these approaches cannot be employed to analyze shale because of its low porosity and ultra-low permeability. In recent years, some scholars have experimentally studied the stress sensitivity and permeability of shales. However, little has been done to analyze the stress sensitivity in the context of the microscopic OM morphology and 3D pore nanostructures of shales, which are precisely the most unique factors that determine the reservoir quality in shales.

In this study, a number of Wufeng and Longmaxi samples collected from Well Xike-3 in Xishui County were imaged by FIB-SEM at different ultra-high resolutions. The samples contain materials of interest, including clump-shaped OMs, interstitial OMs, framboidal pyrite, microfractures between the mineral particles, and microfractures between clay platelets. We have qualitatively and quantitatively characterized the 2D morphology and 3D pore nanostructures porosity, pore size distribution, and pore connectivity of shales. The pulse decay permeability (PDP) measurement was also employed to investigate the stress-dependent permeability variation patterns and stress sensitivity of shale under different confining pressures and pore pressures. The results can thus be used to calculate the Biot coefficients of the two aforementioned shale formations. Finally, we combined the matrix and pore characteristics data from FIB-SEM and stress-dependent permeability measurement to analyze the differences in physical properties between the Longmaxi and Wufeng Formations with the Kozeny–Carman (K–C) models. The relevancies of microscopic OM morphology and 3D pore nanostructure characteristics to the difference in stress sensitivity of shales of the two formations were also investigated and rationally explained.

2. Samples and methods

2.1. Samples

Two types of core rock samples, i.e. Longmaxi and Wufeng Formations, were obtained from Well Xike-3 in Xishui County, northern Guizhou, China. The sampling locations were at depths of 618.54 m and 659.16 m, respectively. The studied area is located in the northern Yunnan–Guizhou Depression outside the southern margin of the Sichuan Basin and belongs to the Yangtze Platform. The tectonic evolution of the northern Guizhou is consistent with that of the Yangtze platform area (Zhou et al., 2016a; Zhou and Liang, 2006). There is a great potential for shale gas resources in the Yangtze Platform area. Many scholars have carried out researches in the northern Guizhou to determine the distribution pattern of the Wufeng–Longmaxi Formation black shale in northern Guizhou. It is generally believed that the Wufeng-Longmaxi Formation black shales in the Sichuan Basin and its surrounding areas are mainly deposited near Chengkou County and Xishui County, with a large sedimentary area. The tectonic uplift caused the water body to penetrate deeper and formed a detained anoxic environment, which is ideal for the preservation of OM (Wang, 2013; Ke, 2015; Kang et al., 2018). In this work, it was found that the Upper Ordovician Wufeng Formation–Lower Silurian Longmaxi Formation black shale samples were deep-water shelf deposit with

high organic content and high gas content of 3.7 m^3/t. The original shale cores were processed into two cubic samples (i.e. S1 and S2) and some cylindrical samples. The dimensions of the cubic samples were 10 mm × 10 mm × 3 mm (length × width × height), and the surface of the samples was polished by mechanical treatment and argon-ion milling for FIB-SEM experiments. The dimensions of the cylindrical samples were 25 mm in height and 25 mm in diameter for PDP measurement.

2.2. FIB-SEM and serial section tomography method

At present, with its high resolution, FIB-SEM has been widely used in studying the nanoscale pore throats in shale. In this experiment, a Zeiss Crossbeam 540 FIB-SEM was used to mill the samples and sequentially image the polished sections. The system consists of two components: an ion beam and an electron beam. The high-energy focused gallium ion beam mills the target area at a high voltage of 30 kV, and the electron beam images the newly milled area with the target accuracy (Fig. 1). After 1000 times of milling and imaging, 1000 2D images of the target area of the interior samples were obtained. Then, 3D digital core reconstruction was performed using Avizo reconstruction software to analyze the 3D pore structure inside the target area of the sample.

Before milling and imaging, the electron beam was turned on to scan the polished surface of the sample, based on which, the area containing the object to be studied was selected and marked. Considering the strong heterogeneity in microscale in the shale and the comparison of pore nanostructure data, four regions of interest were selected from the Longmaxi Formation samples (i.e. S1-1, S1-2, S1-3 and S1-4) and two from the Wufeng Formation samples (i.e. S2-1 and S2-2) (Fig. 2). It should be noted that none of these six regions could represent the pore structure and morphology of the entire formation sample. However, they did provide the typical parameters of OM pores within characteristically selected sample volumes.

As the key features of these regions were different, different resolutions were selected according to the research targets. Specifically, since the main research focus was the OM pores, S1-1, S1-2 and S2-1 were imaged at an ultra-high resolution of 4 nm/pixel and the milling thickness were set as 4 nm. Referring to previous studies using FIB-SEM to characterize OMs and OM pores, the resolution of 4 nm/pixel in the three regions at S1-1, S1-2 and S2-1 is sufficiently high to characterize the majority of OM pores, and an imaging region close to 5 μm is sufficient to represent the distribution of OMs (Figs. 2e and 3). Wang et al. (2019) determined the REV of each phase at different scales for a typical Longmaxi Formation sample by multiscale tomography methods with pixel size ranging from 10 nm to 3.25 μm. Their results showed that the size of a RVE cube at a pixel size of 10 nm is 4–5 μm. S1-3 contained framboidal pyrite and had a high resolution of 4 nm/pixel, under which OM pores between pyrite microcrystalline particles can be identified, but a thickness of 10 nm was selected in order to expand the volume of S1-3. The main research focuses of S1-4 were the microfractures and interparticle pores developed between clay minerals, while S2-2 contained framboidal pyrite and a microfracture. Both cases had a lower resolution of 10 nm/pixel and were divided into 10 nm slices (Table 1). The surface of the milling image was defined as the *x-y* plane, and the distance interval between successive milling images was defined as the increment on the *z*-plane.

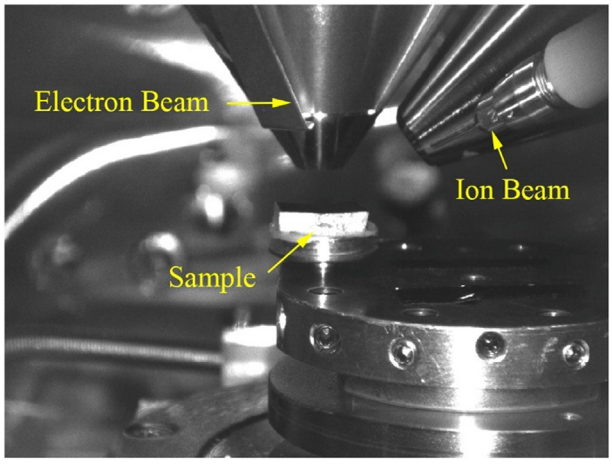

Fig. 1. Operational diagram of FIB-SEM dual-beam system.

2.3. PDP measurement

Among various laboratory measurements of rock permeability, PDP measurement is currently the most applicable one to tight rocks, such as shales. The experiments were conducted with CoreLab PDP-200 permeameter, which is featured by its high accuracy, at a fixed indoor temperature of 22 °C.

Considering the hardware limitations of the pressure loading conditions of the PDP equipment and the original ground stress conditions of the shale cores, the pore pressure was set in the range of 5–13 MPa, and the confining pressure was above 11 MPa. A series of experiments was conducted on the rock samples of the Wufeng and Longmaxi Formations under different confining pressures and pore pressures step by step by determining the confining pressure, respectively, to investigate the stress-dependent permeability of shale in different formations. Thirty six tests were conducted in total. The axes of the cylindrical shale samples were all made parallel to the bedding plane of the shale. Two groups of three samples with similar bedding morphology in the Longmaxi and Wufeng Formations were tested at a pore pressure of 9 MPa and a confining pressure of 11 MPa. The results were similar. Thus, one sample from each group was selected for analysis of the stress-dependent permeability.

3. Results and discussion

3.1. 2D and 3D imaging and characterization of pore structures

In this work, two marine shale samples S1 and S2 were analyzed based on FIB-SEM. The 2D images obtained from the SEM showed that a large amount of framboidal pyrites were visible in both S1 and S2, indicating that both samples were mainly formed in deep-water shelf environment. Although the origin of framboidal pyrite is still controversial, it is generally considered to be the product of chemical deposition in anoxic environment (Schieber and Baird, 2001; Schieber, 2002). The framboidal structure is generally considered to be a unique feature of early pyrite, and its diameter is affected by hydrodynamic effects and greigite development. In addition, the presence of framboidal pyrite could also suggest the reduction of water content at that time, which was beneficial for the preservation of OMs (Liu et al., 2016). The comparison of the scanned images showed that both S1 and S2 were rich in OM, while the morphological distribution of OM was distinctly different. S1 had a large amount of interstitial OMs as strips, while OMs in S2 were mostly scattered blocks (Fig. 3).

The 2D SEM images showed that nanopores, especially OM pores and mineral matrix pores, were abundant in both S1 and S2, and some microfractures also existed. To classify the internal pores

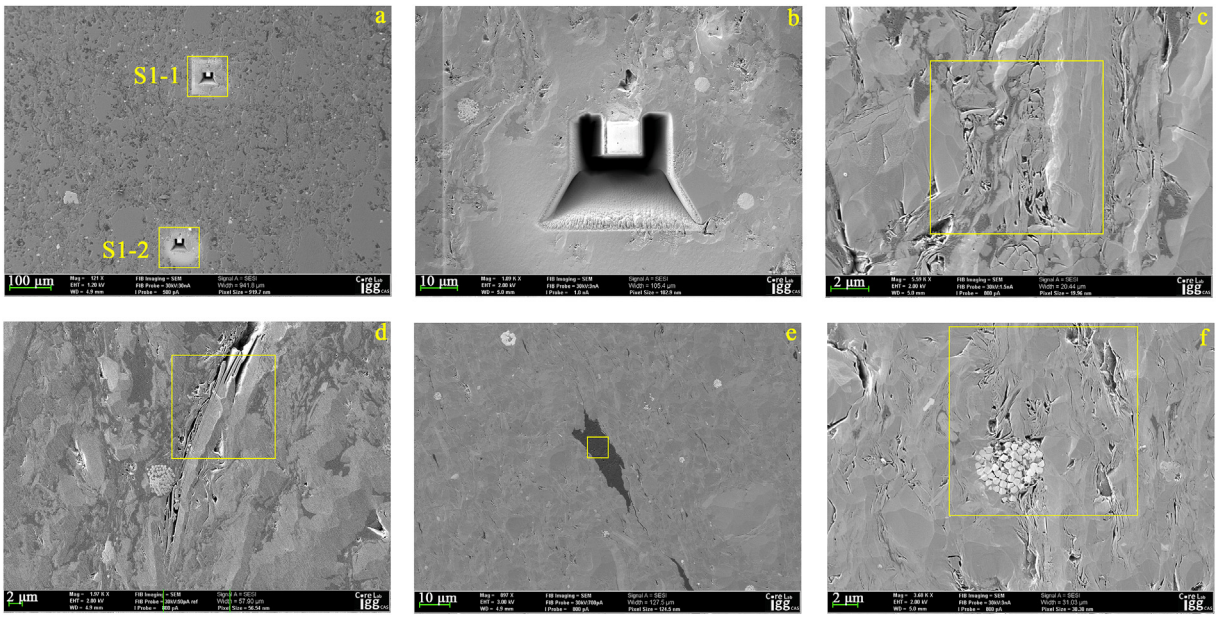

Fig. 2. 2D SEM images of the six regions of interest: (a) S1-1 and S1-2, (b) S1-2, (c) S1-3, (d) S1-4, (e) S2-1, and (f) S2-2.

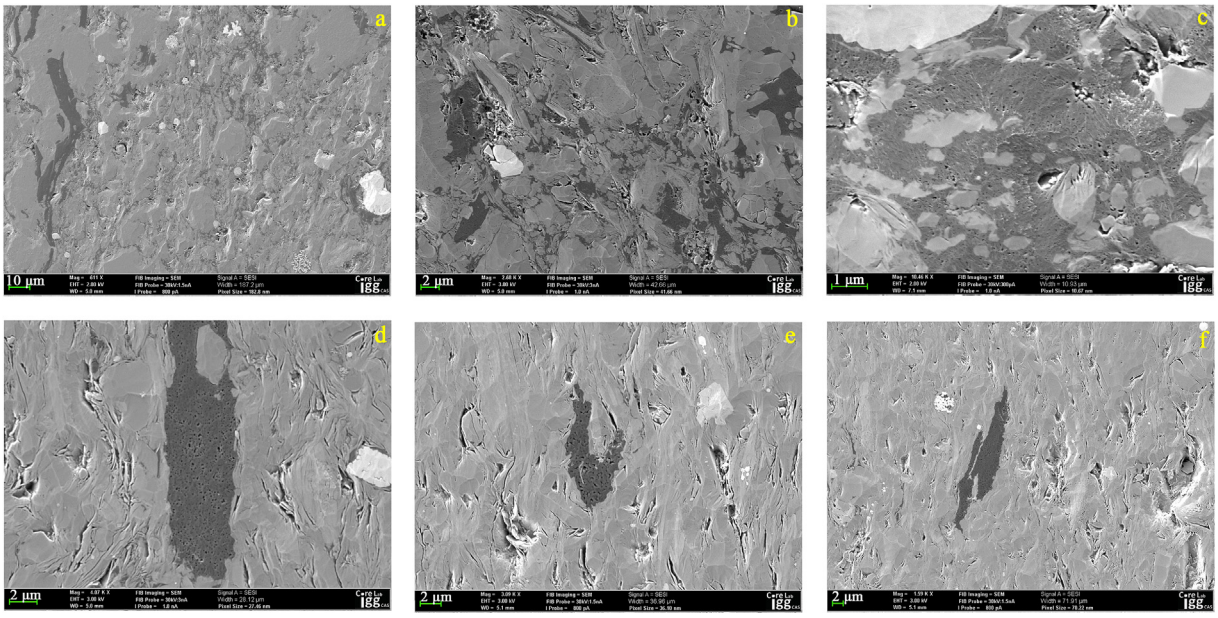

Fig. 3. SEM images showing 2D morphology of OMs and OM pores: (a)–(c) Longmaxi samples and (d)–(f) Wufeng samples.

of shale reservoirs, the classification method by Loucks et al. (2012) has been employed in this study to group the internal nanopore structure of samples into four types: OM pores, interparticle (interP) pores, intraparticle (intraP) pores, and microfracture pores.

OM pore is a special type of pore that has a significant impact on the quality of shale reservoirs, which belongs to intragranular pore developed inside the OM. Due to the uneven distribution of OM and strong heterogeneity, OM pores have different shapes, such as circular, oval, triangular, and other irregular shapes (Fig. 3c–f). In general, the OM pore size of the Longmaxi Formation sample (S1) is smaller than that of the Wufeng Formation sample (S2). The OM in S1 mainly has developed round or bubble-like pores, which are consistent with the pore morphology of the Longmaxi Formation samples at Qilong Section and Fuling shale gas field in the southern Sichuan Basin, China (Wang, 2013; Yang et al., 2017). Considering the importance of OM pores in shale reservoirs and gas flow behavior, the 3D structure, pore connectivity, and specific data will be discussed in detail in Sections 3.1 and 3.2.

InterP pores are the primary pores in the sample, which are usually polygonal and elongated, mainly developed at the contacting areas of mineral particles. The size of interP pores is usually larger than that of OM pores, and some interP pores are filled with OM pores. Fig. 4a and b shows the interP pores together with the surrounding clay. This is because when the plastic clay minerals come into contact with the brittle mineral particles, the clay platelets will deform around the brittle particles, creating new pores. Similarly, interP pores were also developed between clay platelets due to the transformation and compaction (Fig. 4f). IntraP

Table 1
Pore morphology parameters of 3D reconstruction models in the six regions of samples.

Region ID	S1-1	S1-2	S1-3	S1-4	S2-1	S2-2
Formation	Longmaxi	Longmaxi	Longmaxi	Longmaxi	Wufeng	Wufeng
Pixel dimension (nm × nm × nm)	4 × 4 × 4	4 × 4 × 4	4 × 4 × 10	10 × 10 × 10	4 × 4 × 4	10 × 10 × 10
Model dimension (μm × μm × μm)	4.8 × 4.8 × 4	4.8 × 4.8 × 4	4.8 × 4.8 × 10	10 × 10 × 10	4.8 × 4.8 × 4	10 × 10 × 10
Total pore volume (μm^3)	2.75	1.06	0.77	4	4.72	1.14
Total pore area (μm^2)	557.23	184.03	166.95	457.5	343.59	127.59
Porosity (%)	2.98	1.15	0.33	3.14	5.13	0.14
SSA (μm^{-1})	202.67	174.38	215.97	114.48	72.74	111.76
Maximum pore radius (nm)	166.09	252.7	187.4	395.39	1310.34	377.88
Minimum pore radius (nm)	4.96	4.96	6.74	12.41	4.96	12.41
Average pore radius (nm)	23.33	28.22	14.3	34.11	23.93	27.04
Standard deviation of pore radius	16.98	17.2	10.98	20.68	44.15	22.19
Total number of pores	133879	33944	124644	73954	11019	2074

Note: SSA denotes the specific surface area.

pores mainly include the intercrystalline pores within framboidal pyrite, the pores of the pyrite mold, and the dissolution pores in the mineral particles (Fig. 4). High-resolution SEM images show that most of the pores between the pyrite crystal particles within framboidal pyrite are filled with OM pores, with few intercrystalline pores (Fig. 4c and d). Framboidal pyrites are irregular aggregates of early sedimentary pyrites under shallow compaction (Wilkin et al., 1996). Dissolution pores are mainly developed by the dissolution of minerals such as carbonate by organic acids in the process of hydrocarbon generation and expulsion of OM. The intragranular dissolution pores are generally clustered but not connected, which cannot be used as an effective storage space for shale gas (Fig. 4e). Microfractures are important for gas storage in shale reservoirs, and more importantly, they can effectively connect isolated pores and improve the permeability of gas flow in shale reservoirs (Curtis, 2002; Gale at al., 2007). The microfractures between clay platelets shown in Fig. 4f are not filled with OM pores, which may be developed during the dehydration and transformation of clay minerals. They can form a network of fracture system which can increase the gas permeability in shale reservoirs.

The image datasets obtained by FIB-SEM were first cropped and enhanced by filter processing to remove noise, and then imported into Avizo imaging software for 3D reconstruction. In the 2D SEM images, gray values (0–255) for different phases were used to accurately segment the pore and fracture phase (0–75), organic phase (76–100), mineral phase (100–200), and pyrite (200–255). We reconstructed the 3D structures of the six regions (i.e. S1-1, S1-2, S1-3, S1-4, S2-1 and S2-2). Figs. 5–10 show the visualized and quantified 3D reconstruction models of the six regions reconstructed from the datasets of 1000 sequential FIB-SEM images. Table 2 summarizes the volume fractions of the pore, organic, and mineral phases of the six regions.

The 3D reconstruction models of S1-1 and S1-2 both have ultra-high resolution of 4 nm/voxel. They were selected from the organic-rich regions of interest of the Longmaxi Formation sample, and were used to study the structural characterization of OM pores. S1-1 represents the clump-shaped OMs wrapped on the surface of the clay minerals, while S1-2 represents the interstitial OMs between the clay mineral particles (Figs. 5 and 6). Figs. 5b and 6b show the 3D structure of multiple phases, such as the organic (green), phase (red), and mineral phases (yellow) after segmentation. After data processing, we found that all the collected pores in these two areas were OM pores. It can be seen from Figs. 5c and 6c that the OM pores are abundant with small size and relatively uniform shape. Most of small pores are close to spherical, elliptical and bubbly in shape, while the larger ones are irregular. The pores are basically isolated from each other, and do not have visually good connectivity. The shape and size of OM pores are related to factors such as organic thermal maturity and shale burial depth. Shales with high total organic carbon (TOC) are more likely to develop such bubble-like small circular pores through the evolution of hydrocarbon generation and expulsion process. The result is consistent with some published data related to the OM pore structure of the Longmaxi Formation in the southern Sichuan Basin, China (Zhou et al., 2016b; Ju et al., 2017; Yang et al., 2017). The models shown in Figs. 5d and 6d are based on the statistics of each pore volume, and the pores were rendered in four colors according to the pore volume contribution. This model can to some extent reflect the uniformity and connectivity of pore distributions. Specific quantitative analysis of porosity, pore size, pore volume contribution, and pore connectivity will be described in detail in Section 3.2.

The 3D model of S1-3 was imaged and reconstructed with an anisotropic voxel size of 4.8 μm × 4.8 μm × 10 μm. The region was mainly composed of mineral matrix and a small amount of free OM, including a piece of framboidal pyrite (highlighted in blue in Fig. 7b). Similar to the pores in S1-1 and S1-2, all the pores in the reconstruction model were OM pores, including the microcrystalline particles of framboidal pyrite, which were all filled with OM and OM pores. As can be seen in Fig. 7c, the OM pores inside the slit-shaped OM are freely interspersed between the mineral matrixes and have smaller pore sizes than pores developed in organic-rich regions (i.e. S1-1 and S1-2). They are more isolated than the pores in the concentrated OM in S1-1. It is interesting to note that although the pores between the framboidal pyrite microcrystalline particles are completely filled with OM and OM pores, the OM surrounding the microcrystalline particles developed some large OM pores (Fig. 7d). By comparing the 3D structural models of OM pores between framboidal pyrite microcrystalline particles and pores inside the free OM, it can be found that the former obviously has a larger pore volume contribution and potentially better connectivity, which can effectively form a gas reservoir. The pore structure characterization and image datasets of this framboidal pyrite can provide some new insights into multiscale modeling of 3D digital cores of shale in the future.

S1-4 contains some OM pores and 19 microfractures between clay platelets, which were imaged at 10 nm/voxel. These microfractures are about tens to hundreds of nanometers in width and are completely penetrated along the *z*-axis direction (Fig. 8). Small portion of these fractures were filled with OMs and small bubble-like OM pores. In order to better understand the microfractures in combination with the 3D structure, Table 3 lists the volume, SSA and total porosity of the microfractures and pores in S1-4. These microfractures between clay platelets are generally formed by dehydration and transformation of clay minerals, and there is no obvious connection between them and the surrounding OM pores or the intragranular pores of minerals. However, it can be seen from

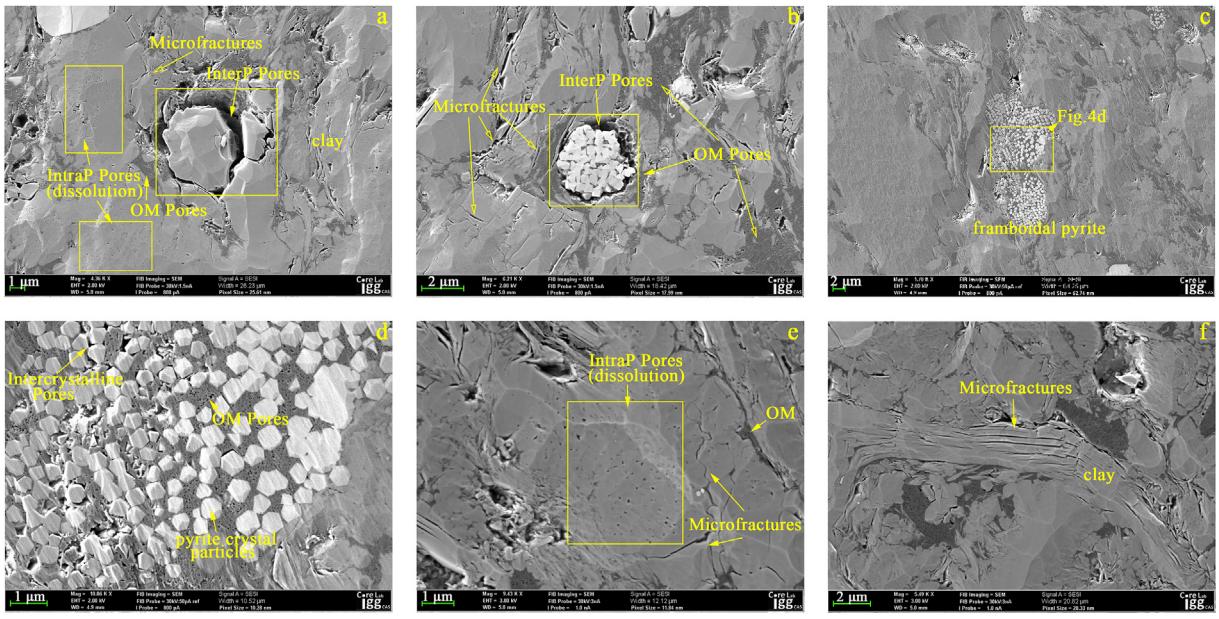

Fig. 4. SEM images showing the 2D morphology of OM pores, interP pores, intraP pores, and microfractures: (a) InterP pores of mineral particle, intraP pores developed by dissolution, microfractures and OM pores; (b) InterP pores of framboidal pyrite, microfractures and OM pores; (c) Framboidal pyrite; (d) Framboidal pyrite filled with pyrite crystal particles, OM pores and intercrystalline pores; (e) IntraP pores developed by dissolution and microfractures; and (f) Microfractures between clay platelets.

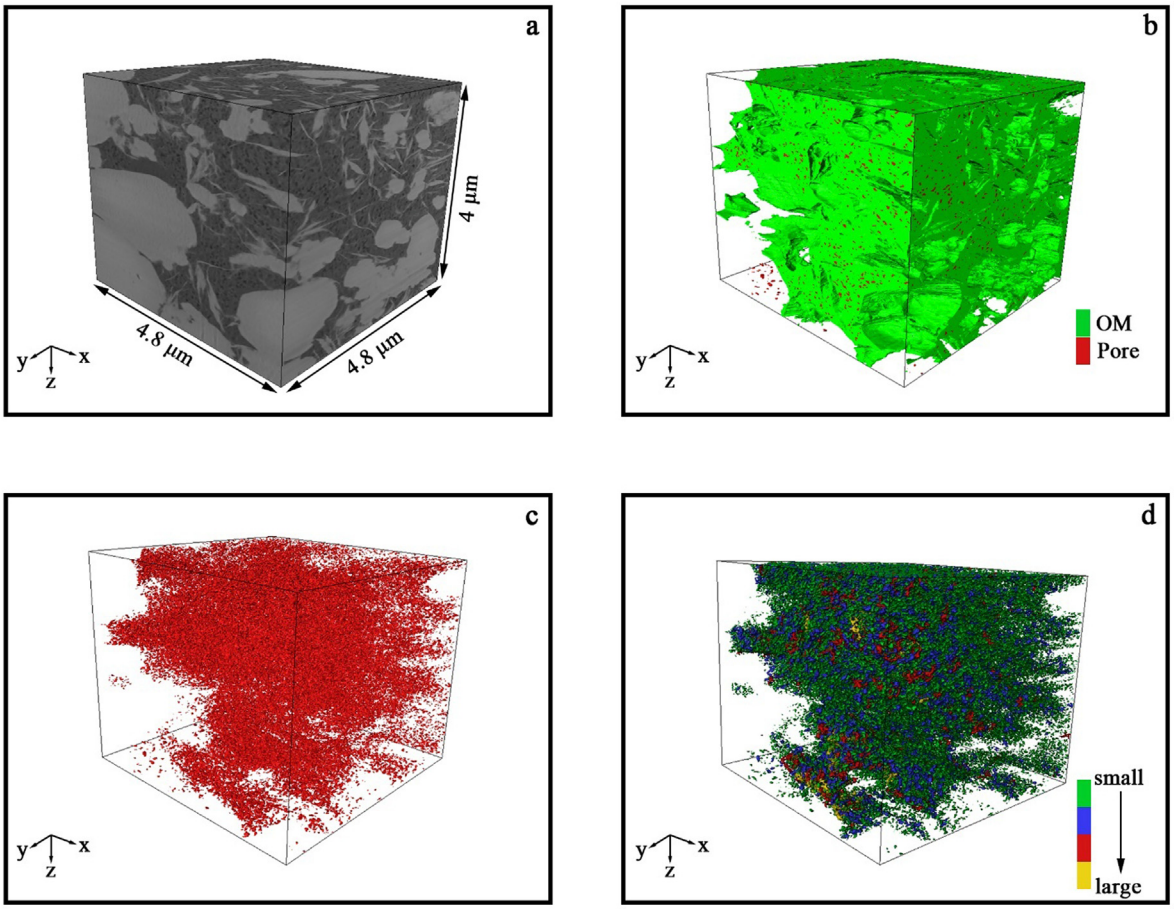

Fig. 5. 3D reconstruction models for S1-1 with dimensions of 4.8 μm × 4.8 μm × 4 μm (length × width × height): (a) Greyscale model; (b) Multiphase model showing OM (green) and pores (red); (c) Pore structure; and (d) Pore volume distribution (green, blue, red and yellow represent the contribution of pore volume from small to large).

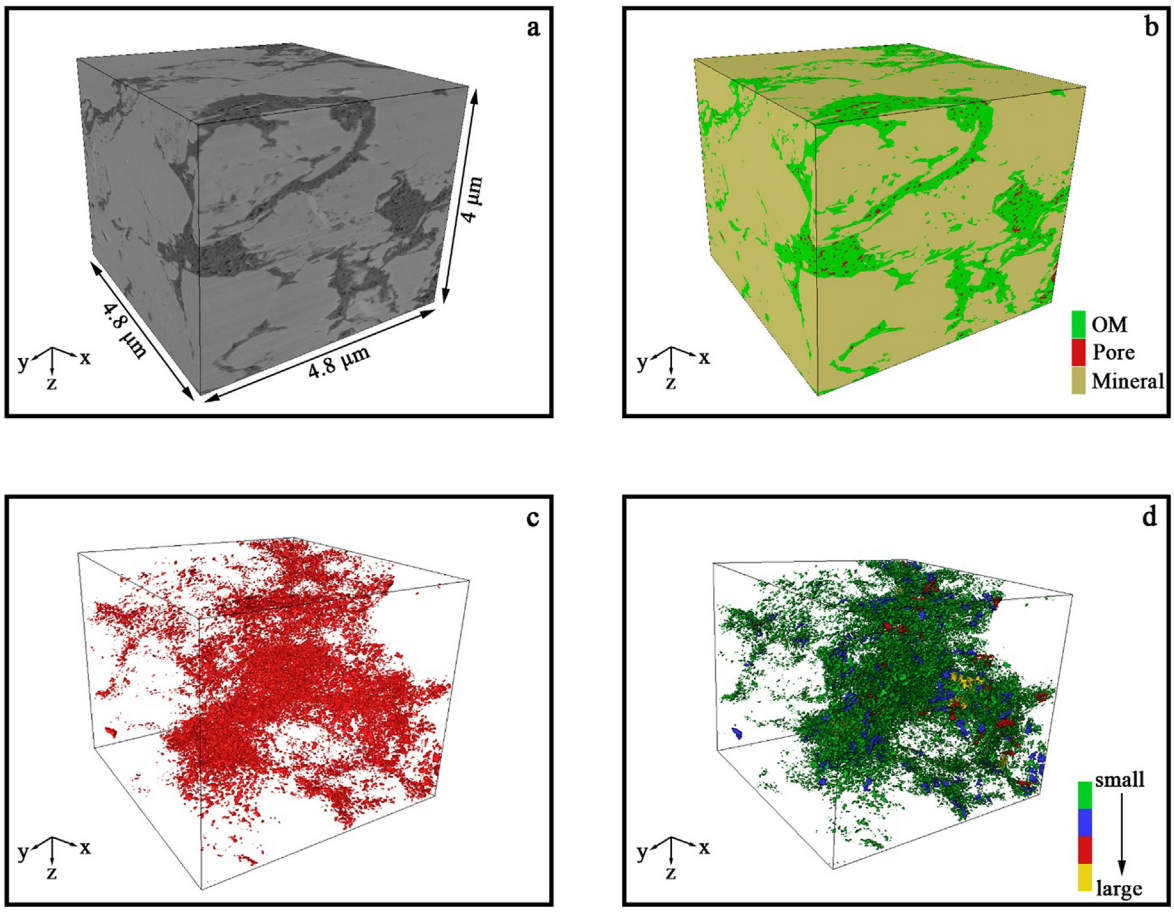

Fig. 6. 3D reconstruction models for S1-2 with dimensions of 4.8 μm × 4.8 μm × 4 μm (length × width × height): (a) Greyscale model; (b) Multiphase model showing OM (green), pores (red), and the basic mineral matrix (yellow); (c) Pore structure; and (d) Pore volume distribution.

Fig. 8d that the OMs in the center and periphery of the fractures developed some OM pores with large volume in this region, which might be marginal pores between the OMs and the fractures.

Concerning the S2-1 region (Wufeng Formation), its OMs continuously developed into clumps and were imaged at 4 nm/voxel. The region entirely consisted of OMs and OM pores (Fig. 9b). The shape and distribution of OM pores in this region are significantly different from those in S1-1 and S1-2 (Longmaxi Formation). The OM pores in S2-1 region have larger pore size, and their shape is mainly irregular polygon with edge shrinkage and better connectivity (Fig. 9c and d). The factors that cause these differences may be TOC, organic thermal maturity, burial depth and structural development. The OM pore morphology of S2-1 is consistent with the published data of the Wufeng Formation in Fuling shale gas field, southern Sichuan Basin, China (Chen et al., 2019).

Similar to S1-3, the S2-2 region contained mineral matrix and a small amount of free OMs, as well as two pieces of framboidal pyrite (Fig. 10b). In this region, there are large irregular intraP pores inside the framboidal pyrite, small OM pores with regular shapes and isolated distribution inside the free OMs, and seven microfractures between the mineral particles. Comparing its morphology and distribution of OM pores with those of S2-1, it was found that in S2-2 region, the OM pores inside the slit-shaped OM that were freely interspersed between the minerals were much smaller than the pores in the concentrated OMs. They were mostly isolated in the form of bubbles with significantly worse connectivity. In order to better observe the OMs and pore morphology between framboidal pyrite microcrystalline particles, two pieces of framboidal pyrite were separately segmented and imaged (Fig. 10e–h). Similar to S1-3, the two pieces of framboidal pyrite in S2-2 region also contained large clustered connected pores, while these pores were not all OM pores, with some intercrystalline and moldic pores.

3.2. Pore size distribution and pore connectivity

We statistically analyzed the image datasets of S1-1, S1-2, S1-3, S1-4, S2-1 and S2-2. The morphology parameters of the pore structural models were summarized in Table 1. As shown in Figs. 11 and 12, 12 charts were plotted to illustrate the pore size distributions.

As shown in Table 1, the average radius of OM pores in the organic-rich region of the Longmaxi Formation represented by S1-1 is 23.33 nm, which is slightly smaller than the results of Longmaxi Formation in Fuling shale gas field, southern Sichuan Basin, China (Zhou et al., 2016b; Ju et al., 2017), while the average radius of OM pores in the organic-rich region of the Wufeng Formation represented by S2-1 is 23.93 nm. However, the results in Section 3.1 showed that the OM pore morphology and distribution of S1-1 and S2-1 are quite different. Thus, Figs. 11 and 12 are used to further analyze the pore size distribution.

Unimodal pore size distributions by pore number and pore volume are observed for the four regions (i.e. S1-1, S1-2, S1-3 and S1-4) of the Longmaxi Formation (Figs. 11 and 12). As can be seen in Fig. 11a and b, the OM pores in the two organic-rich regions are mostly those with radius less than 40 nm, accounting for about 85% of the total number of pores. However, these pores contribute less

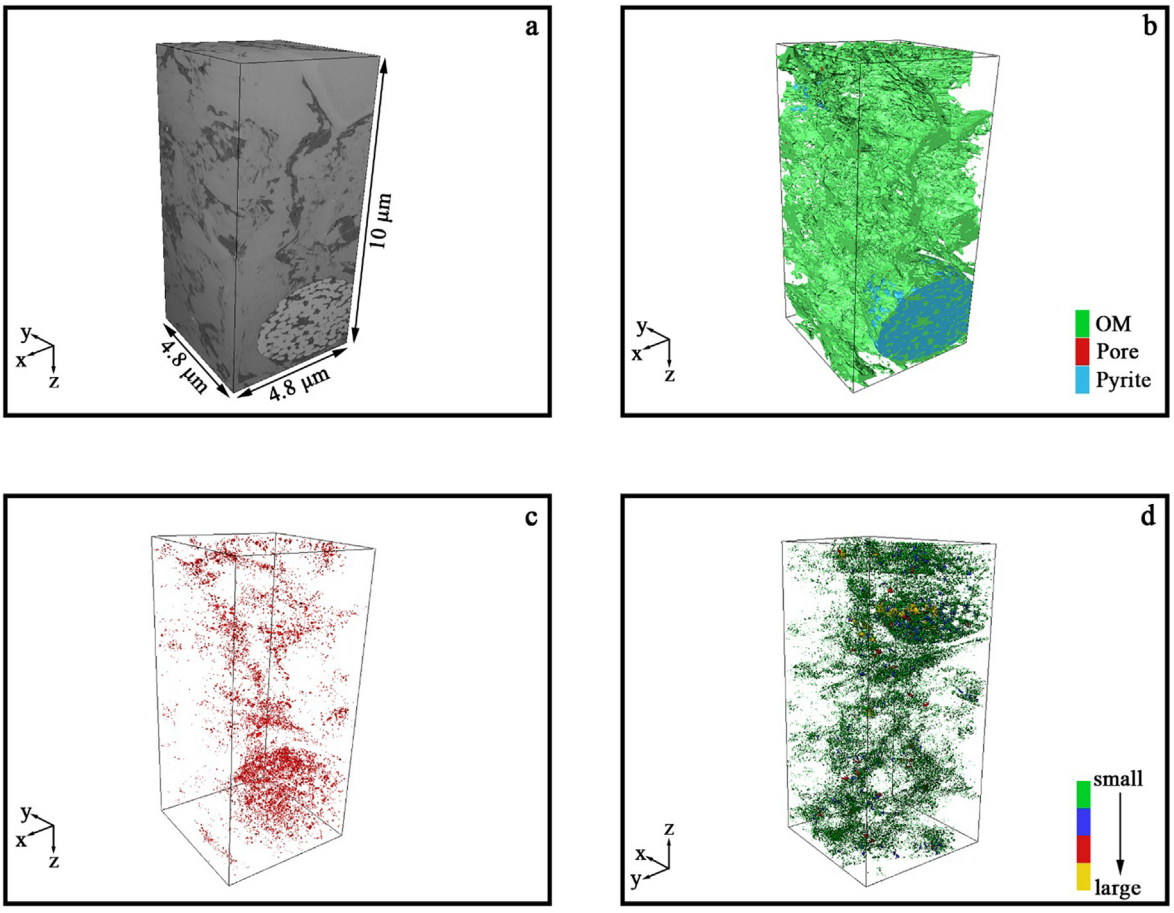

Fig. 7. 3D reconstruction models for S1-3 with dimensions of 4.8 μm × 4.8 μm × 10 μm (length × width × height): (a) Greyscale model; (b) Multiphase model showing OM (green), pores (red), and pyrite (blue); (c) Pore structure; and (d) Pore volume distribution.

than 25% of the total pore volume (Fig. 12a and b). This finding is basically consistent with the results of the OM pore size distribution of the Longmaxi Formation in Fuling shale gas field (Zhou et al., 2016b; Ju et al., 2017). Our results also show that there are a large number of pores with less than 10 nm, which may be resulted from the high resolution used in this study. Goral et al. (2019a) studied the organic-rich regions of the Vaca Muerta shale in Argentina with FIB-SEM (resolution of 2.5 nm) and reconstruction technology. Their results showed that the radius of 95% of the pores is less than 75 nm, which is smaller than ours. Pores with radius less than 10 nm account for more than 50% of total number of pores in S1-3 (Fig. 11c), indicating that there are many micropores in the slit-shaped OM which are free from interstitial minerals in the Longmaxi Formation. The SSA values in Table 1 show that the micropores have a significant contribution to the SSA, while large pores have a significant contribution to the pore volume. Due to the existence of microfractures between clay platelets, the OM developed large pores in some fractures, contributing to about 8% of the pore volume in S1-4 (Figs. 11d and 12d).

The pore size distribution of the region S2-1 in the Wufeng Formation is different from that in the Longmaxi Formation that 85% of the pores contribute to only 0.5% of the pore volume, and 11 large pores with pore size greater than 500 nm amount to more than half of the pore volume (Figs. 11e and 12e). This result is completely different from the OM pore size distribution of the Wufeng Formation in Fuling shale gas field discovered by Yang et al. (2017): Yang's results showed that pores with size less than 20 nm contribute to 88% of the pore volume. Compared with that of the Longmaxi Formation, the pore size distribution of the Wufeng Formation is more uneven, which is reflected by the largest standard deviation of pore radius of S2-1 in Table 1. The OM pore size in Longmaxi Formation is mainly distributed between 20 nm and 80 nm (where the slope of cumulative volume percentage curve is large), while the pore volume of Wufeng Formation is more contributed by macropores. In S2-1 region, there are a large number of micropores with radius less than 20 nm and large pores with radius more than hundreds of nanometers, indicating a good adsorption capacity of shale gas and accumulation space.

The porosity and connectivity of pores, especially the OM pores, are important factors for evaluating the development potential of shale gas reservoirs. High porosity and good connectivity indicate rich accumulation and high migration of shale gas. Zhang et al. (2019) assessed pore structure and complex pore connectivity by analyzing 600 contiguous high-resolution SEM images of shale, and the results suggested that the REV describing the pore connectivity of shale is about 4 μm. After processing the original image datasets, the connected pores and fractures in the investigated regions were segmented and the reconstruction imaging was performed to visualize the connected pores morphology inside the sample (Fig. 13). Most of the OM pores in the Longmaxi Formation are isolated from each other, while a few are connected in clusters, with poor overall connectivity (Fig. 13a and e). Since the OM pore connectivities in S1-2 and S1-3 are similar, they are not listed here. The fractures in S1-4 throughout the entire area along the *z*-axis

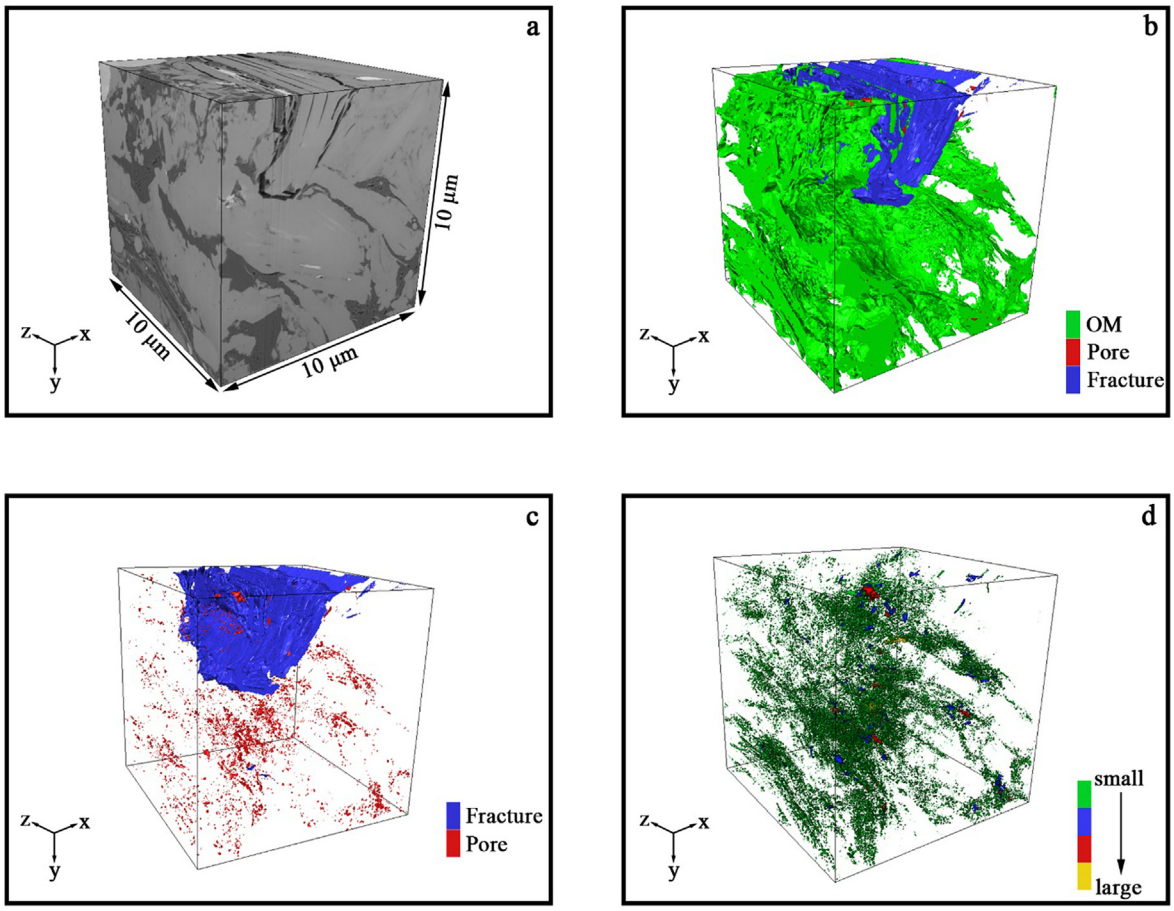

Fig. 8. 3D reconstruction models for S1-4 with dimensions of 10 μm × 10 μm × 10 μm (length × width × height): (a) Greyscale model; (b) Multiphase model showing OM (green), pores (red) and fractures (blue); (c) Fracture (blue) and pore (red) structure; and (d) Pore volume distribution.

direction greatly increase the connectivity of the region (Fig. 13b and f). The organic-rich region in the Wufeng Formation showed good connectivity, and the connected irregularly shaped OM pores distributed along the *y*-axis direction (Fig. 14c and g), which has not been observed in previous studies. However, the slit-shaped OM between the mineral matrixes of Wufeng Formation did not show good connectivity (Fig. 13d and h).

Due to the strong anisotropy of the shale and the large differences between the selected regions, we unified the porosity and connectivity parameters of regions with different research objects, as shown in Table 4. For example, although both are taken from the large continuous organic-rich regions, S1-1 and S2-1 have different OM contents. In order to study the OM pores in the organic-rich region, the porosity was converted into the ratio of OM pore volume to the OM volume. By comparing the converted OM porosities, it is found that the porosities of OM pores in the Longmaxi and Wufeng Formations are similar and larger than those reported by Ju et al. (2017) and Huang et al. (2012). This result indicates good gas adsorption capacity and storage property of OM pores in the Longmaxi–Wufeng Formation in the northern Guizhou, China. The large effective porosity of the clumped OMs of the Wufeng Formation suggested good gas migration performance.

3.3. Permeability and OM pore characteristic parameters

First, a pore pressure value of 9 MPa was selected. Then permeability measurements were conducted on the samples of Longmaxi and Wufeng Formations under the condition that the confining pressure values increased step by step gradually and were higher than the pore pressure value of 2 MPa–22 MPa and 38 MPa, respectively. The results are shown in Fig. 14, and the horizontal coordinate 'pressure difference' is the difference between the confining pressure and the pore pressure.

Our analysis showed that the variations of permeability versus pressure difference (or confining pressure) for the Longmaxi and Wufeng samples can be well fitted by exponential functions. By fitting with the least squares regression method, the permeability values were obtained as 1.0624×10^{-3} mD and 1.4501×10^{-2} mD for the Longmaxi and Wufeng samples, respectively, at a zero pressure difference value. This was also the closest to the zero-confining pressure condition under which we conducted the FIB-SEM imaging experiments.

There is a strong dependence of permeability on physical parameters such as porosity and SSA. However, due to the complex pore structures of reservoirs, especially the tight reservoirs, it is difficult to establish an accurate model to describe this relationship. As a commonly used method, the K–C model is expressed as

$$K = \frac{\varphi^3}{c\tau^2 S^2} \tag{1}$$

where φ is the porosity, S is the matrix SSA, c is the K–C constant, and τ is the pore tortuosity. For simple capillary tube models, $c = 2$; and for tight reservoirs, the value of τ usually ranges from 1.5 to 3. In this research, we took the value $c\tau^2 = 5$.

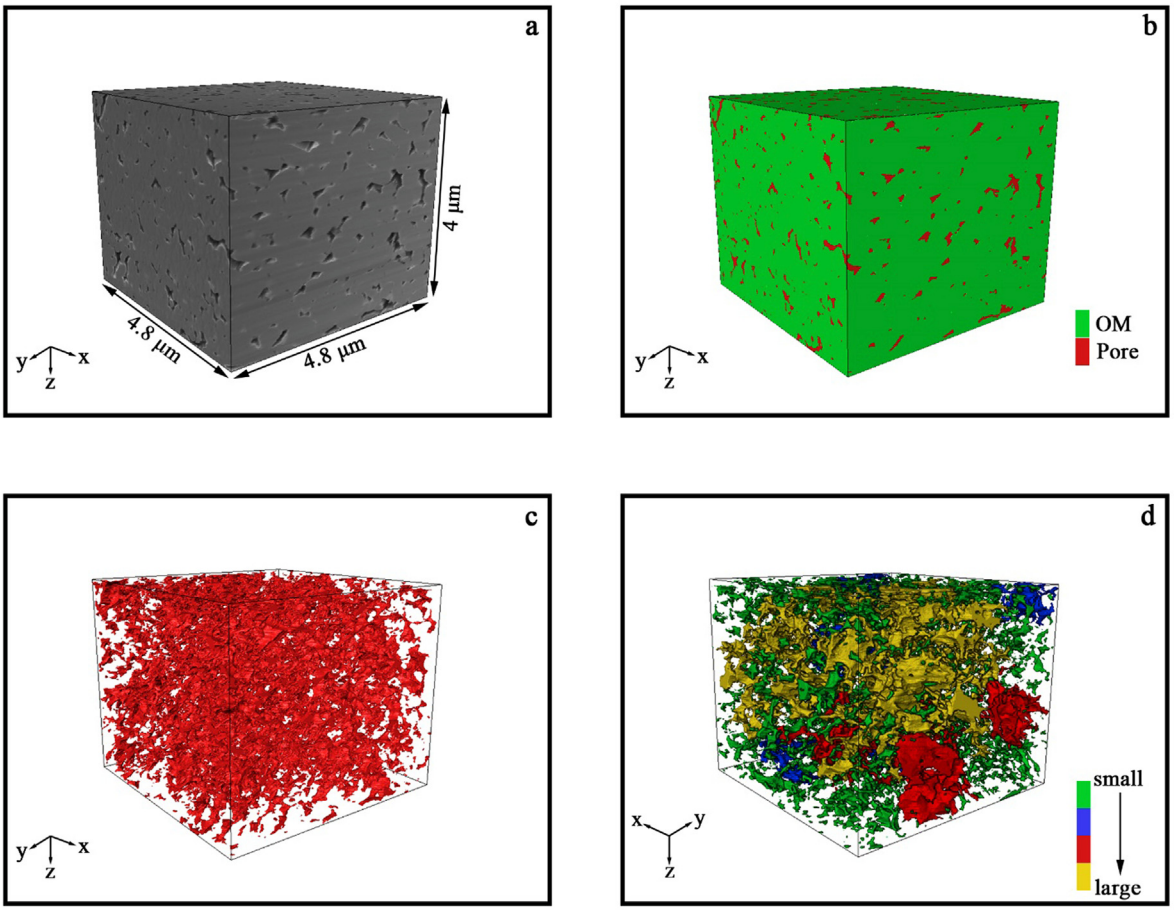

Fig. 9. 3D reconstruction models for S2-1 with dimensions of 4.8 μm × 4.8 μm × 4 μm (length × width × height): (a) Greyscale model; (b) Multiphase model showing OM (green) and pores (red); (c) Pore structure; and (d) Pore volume distribution.

Latief and Fauzi (2012) proposed modified power laws of porosity or multiplications by tuning parameters in the K–C equation and applied the modified K–C equations to predicting rock permeability, which resulted in well-matched curves. We have selected three of these modified K–C equations that fit the characteristic parameters of our shale samples to calculate the permeability of the Longmaxi and Wufeng samples for regions S1-1 and S2-1 (Table 5). The permeability of the Wufeng samples was 10.5, 11.6 and 17.9 times higher than that of the Longmaxi samples, while the permeability of the Wufeng sample at a zero pressure difference value obtained by fitting the experimental data on permeability was 13.6 times higher than that of the Longmaxi sample, which corroborated each other. It can be seen that for the Wufeng–Longmaxi Formation reservoir with high organic content and well-developed OM pores, the macroscopic permeability strongly depends on the permeability of OM pores.

3.4. Stress-dependent permeability and Biot coefficient

The measurements of permeability in Section 3.3 were followed by an additional set of measurements with a confining pressure value of 15 MPa and the pore pressure values being sequentially 2 MPa, 4 MPa, 6 MPa, 8 MPa and 10 MPa lower than the confining pressure values. The results are shown in Fig. 15c and d. The relationship of permeability versus pore pressure can also be fitted by exponential functions.

The stress sensitivity is defined as the effect of pressure difference on pore structures due to the influences of matrix stress and pressure of fluids within the pores, which is reflected by the amplitude of variation of the permeability with the change of stress. In this paper, the decline curve of permeability and the exponential value of the fitted exponential functions (Figs. 14 and 15) indicated the stress sensitivity of permeability. The stress sensitivity of Wufeng samples in the permeability tests was significantly lower than that of Longmaxi samples. This may be due to several possibilities: (1) The OMs of Longmaxi samples were mostly in the form of strips and freely distributed among clay minerals, while the OMs of Wufeng samples were mostly in the form of independent scattered blocks. The OM structures of the former were more likely to be compressed and deformed under the pressure difference; (2) The OM pores of Longmaxi samples were in the shape of regular sphere, ellipsoid or bubble (Fig. 5), while the OM pores of Wufeng samples were in the shape of irregular polygon with edge shrinkage with obvious pore structure anisotropy (Fig. 9). The stress sensitivity of the latter's pore structures might be lower; (3) Under the joint loading of confining and pore pressures, the irregularly connected pore structures of Wufeng samples were crushed and collapsed, while this process might coalesce pores that are not originally connected, which had a resistance effect on the decrease of stress-dependent permeability.

For oil and gas reservoir rocks, the effective stress is no longer the stress difference between confining and pore pressures, but defined as

$$\sigma_{\text{eff}} = p_{\text{c}} - \alpha p_{\text{p}} \tag{2}$$

where p_{c} is the confining pressure, p_{p} is the pore pressure, and α is the Biot coefficient. Typically, for tight sandstones or shales, $\alpha < 1$.

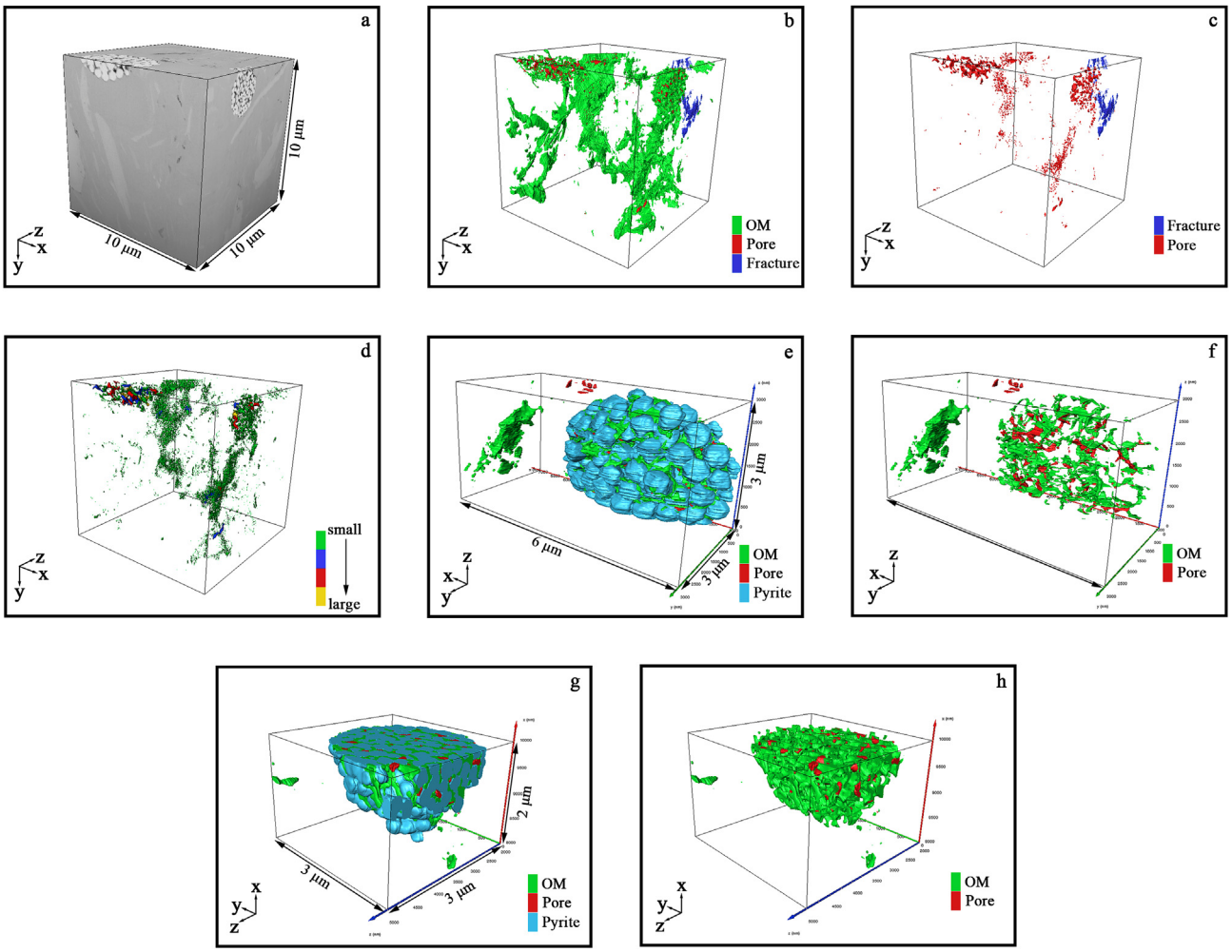

Fig. 10. 3D reconstruction models for (a–d) S2-2 with dimensions of 10 μm × 10 μm × 10 μm (length × width × height) and (e–h) two segmented regions of framboidal pyrite with dimensions of 6 μm × 3 μm × 3 μm (length × width × height) and 3 μm × 3 μm × 2 μm (length × width × height), respectively: (a) Greyscale model; (b) Multiphase model showing OM (green), pores (red) and fractures (blue); (c) Fracture (blue) and pore (red) structures; (d) Pore volume distribution; and (e–h) Multiphase model showing OM (green), pores (red), and pyrite (blue).

Table 2
Volume fractions of the pore, organic and mineral phases within the 3D reconstruction models of S1-1, S1-2, S1-3, S1-4, S2-1 and S2-2.

Region ID	Volume fraction (%)		
	Pore phase	Organic phase	Mineral phase
S1-1	2.98	47.94	49.08
S1-2	1.15	19.67	79.18
S1-3	0.34	15.48	84.18[b]
S1-4	3.14[a]	20.7	76.16
S2-1	5.13	94.87	0
S2-2	0.14[c]	1.43	98.43[d]

Note: [a] 2.74% of fracture, [b] 5.51% of pyrite, [c] 0.025% fracture, and [d] 1.13% pyrite.

In this study, we adopted the differential method to determine the Biot coefficients of Longmaxi and Wufeng samples. The permeability K can be expressed as a function of the effective stress σ_{eff} by

$$K = K\left(\sigma_{\text{eff}}\right) = K\left(p_{\text{c}} - \alpha p_{\text{p}}\right) \tag{3}$$

When K is constant, the corresponding effective stress σ_{eff} is also constant, thus we have

Table 3
Microfracture and nanoscale pore morphology parameters of 3D reconstruction models for S1-4.

Type	Number	Volume (μm^3)	Porosity (%)	SSA (μm^{-1})
Fracture	19	27.44	2.74	17.27
Pore	73,954	4	0.4	114.48

$$\mathrm{d}K = \left(\frac{\partial K}{\partial p_{\text{c}}}\right)\mathrm{d}p_{\text{c}} + \left(\frac{\partial K}{\partial p_{\text{p}}}\right)\mathrm{d}p_{\text{p}} = 0 \tag{4}$$

$$\mathrm{d}\sigma_{\text{eff}} = \mathrm{d}p_{\text{c}} - \alpha \mathrm{d}p_{\text{p}} = 0 \tag{5}$$

Combining Eqs. (4) and (5), following equation can be obtained:

$$\alpha = -\left(\frac{\partial K}{\partial p_{\text{p}}}\right) \Big/ \left(\frac{\partial K}{\partial p_{\text{c}}}\right) \tag{6}$$

Thus, according to the fitted data in Fig. 15, the Biot coefficients of 0.729 and 0.697 were obtained for Longmaxi and Wufeng samples, respectively, which were similar. These values are larger than those for the tight gas sandstone ($\alpha = 0.509$ and 0.612) obtained by Qiao et al. (2011), and smaller than that for the coal shale

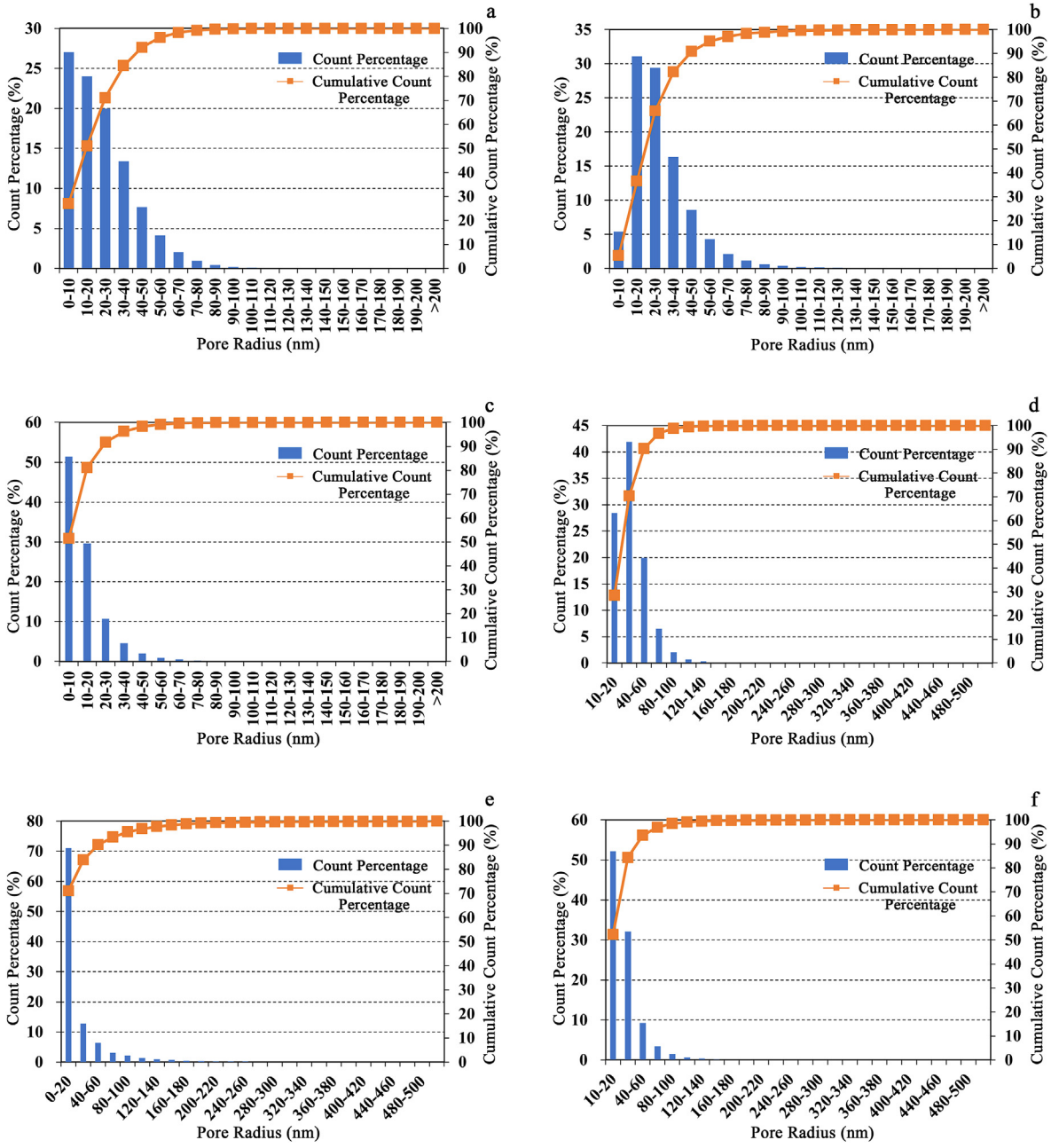

Fig. 11. Statistics of pore size distributions by pore number for (a) S1-1, (b) S1-2, (c) S1-3, (d) S1-4, (e) S2-1, and (f) S2-2.

($\alpha = 0.996$) measured by Zhang and Liu (2018). For shale reservoirs, determination of the Biot coefficient can help researchers obtain the true effective stress and provide guidance on shale gas extraction.

4. Conclusions

We have quantitatively and qualitatively analyzed the pore morphology, porosity, pore size distribution and pore connectivity of Wufeng–Longmaxi Formation using ultra-high nanoscale-resolution FIB-SEM imaging and 3D reconstruction techniques. We have shown that the shale samples had high OM contents and developed a large number of pores, as well as good reduced sedimentary environment and OM storage conditions. Compared with previous researches on the pore characterization of the Wufeng–Longmaxi Formation in the southern Sichuan Basin, China, the OM porosity is larger in this study, though the same pores morphology was observed. Different from the isolated 3D pore structure in the previous researches, the OM pores of the Wufeng Formation in our study showed much better connectivity, which has never been found before. These results indicated good conditions for adsorbed gas and storage space in Wufeng–Longmaxi Formation and potential for shale gas development. The nanoscale pores of the Wufeng and Longmaxi Formations are mainly massive OM pores. The OM pores with radius less than 40 nm account for about 85% in number. We have further shown that OM and OM pore morphology vary greatly in shales of different formations in the same region. The OMs of Longmaxi Formation were mostly in the form of strips

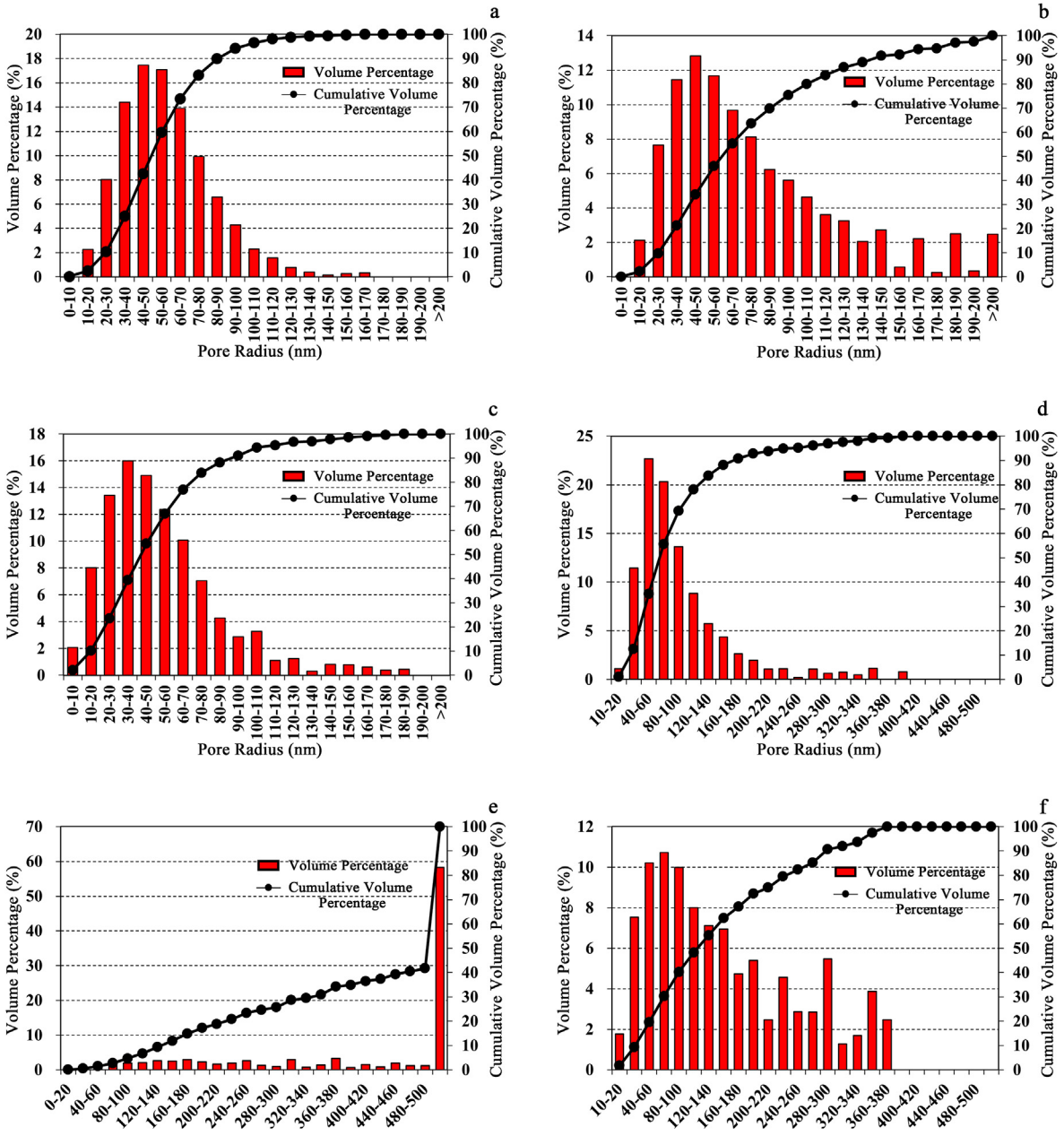

Fig. 12. Statistics of pore size distributions by pore volume of (a) S1-1, (b) S1-2, (c) S1-3, (d) S1-4, (e) S2-1, and (f) S2-2.

and distributed freely among clay minerals, while the OMs of Wufeng Formation were mostly in the form of independent scattered blocks. The OM pores of Longmaxi Formation were isolated from each other, but only locally connected in clusters with small pore size distribution. The OM pores of the Wufeng Formation developed into irregular polygon-shape, and some pores even had radius greater than 500 nm, which significantly improves the pore connectivity of the Wufeng Formation.

We have explored the stress-dependent permeability of shales by conducting four sets of PDP measurement under different confining and pore pressures. The relationships of permeability versus confining pressure and pore pressure for the Longmaxi and Wufeng Formations have been fitted well by exponential functions. We have further analyzed the PDP and the permeability calculated using the K–C model and FIB-SEM pore parameters. The results were in consistent with the permeability difference between the Longmaxi and Wufeng Formations, which indicated that the macroscopic permeability strongly depends on the permeability of OM pores. The stress sensitivity of Wufeng Formation in terms of the permeability was significantly lower than that of Longmaxi Formation, and this has been discussed in detail with respect to the differences in microscopic OM and pore morphological characteristics. Biot coefficients of 0.729 and 0.697 have been obtained for the Longmaxi and Wufeng Formations, respectively.

The results of this study provide new insights into the complex 3D pore nanostructures, fluid migration mechanisms, and stress sensitivity of permeability of the Upper Ordovician–Lower Silurian organic-rich shales. This research could help evaluate the reservoir quality and forecast gas production of shale reservoirs in the

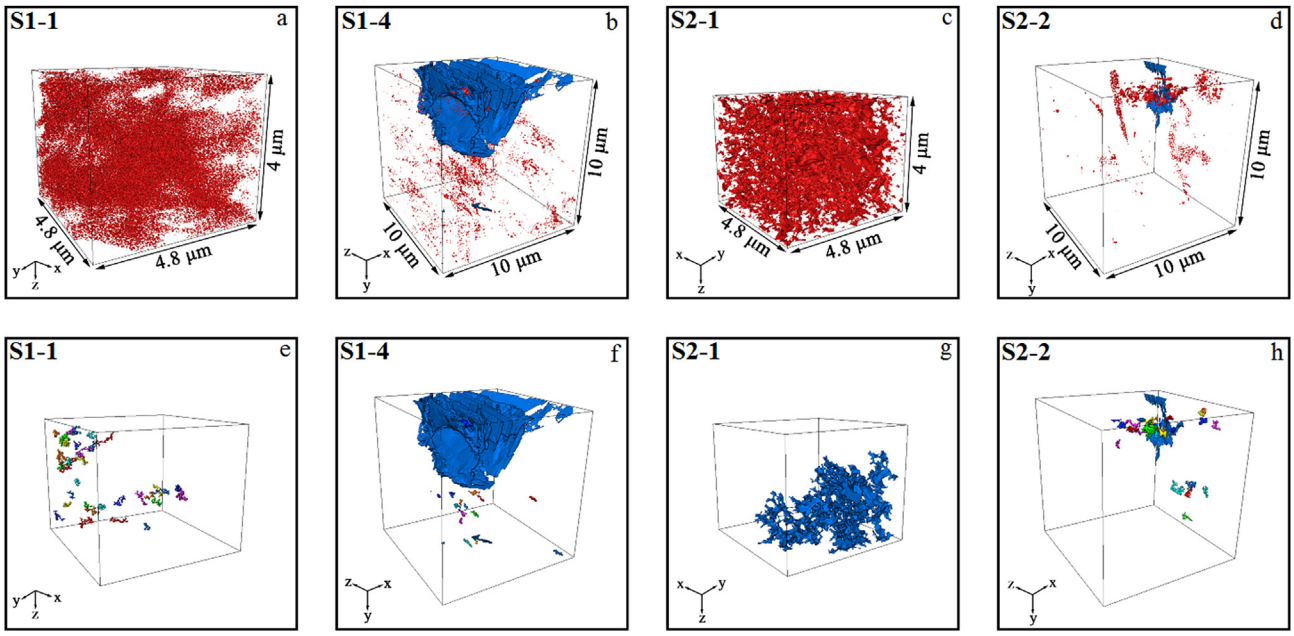

Fig. 13. Comparison of 3D reconstruction models of total porosity (a–d) and effective (connected) porosity (e–h) showing connectivity.

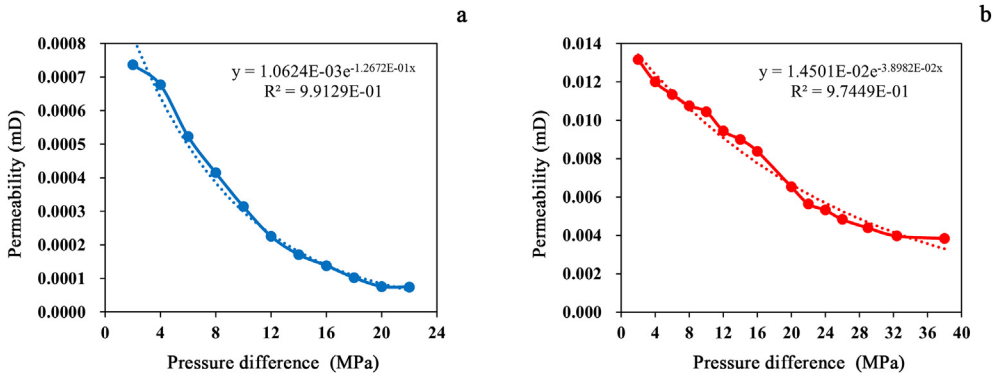

Fig. 14. Permeability versus pressure difference of (a) Longmaxi and (b) Wufeng Formations.

Table 4
Porosity and connectivity parameters of 3D reconstruction models for S1-1, S1-4, S2-1 and S2-2.

Region ID	Formation	Pixel dimensions (nm × nm × nm)	Total porositya (%)	Porosityb (%)	Fracture porosityc (%)	Converted OM porosity (%)	Connected pores percentage (%)	Effective porosity (%)
S1-1	Longmaxi	4 × 4 × 4	2.98	2.98		5.85	1.71	0.05
S1-4	Longmaxi	10 × 10 × 10	3.14	0.4	2.74	5.54	88.02	2.76
S2-1	Wufeng	4 × 4 × 4	5.13	5.13		5.13	24.94	1.28
S2-2	Wufeng	10 × 10 × 10	0.13	0.11	0.02		24.57	0.32

Note: a Porosity of all pores and fractures, b porosity of pores, c porosity of fractures.

Table 5
Permeability of S1-1 and S2-1 calculated by K–C equation.

Region ID	Pore characteristic parameter		Permeability (m^2)		
	φ (%)	S (μm^{-1})	$K = \varphi^3/(c\tau^2S^2)$	$K = 10^{2\varphi}\varphi^3/(c\tau^2S^2)$	$K = 15\varphi^4/(c\tau^2S^2)$
S1-1	2.98	7.566	9.278×10^{-20}	1.064×10^{-19}	4.152×10^{-20}
S2-1	5.13	5.263	9.72×10^{-19}	1.231×10^{-18}	7.472×10^{-19}

northern Guizhou Depression, China. The stress sensitivity and Biot coefficient of shale reservoirs have significant impacts on the production of gas wells. Thus, the role of microscopic OM morphology and 3D pore nanostructures on the stress sensitivity of shale matrix can also help guide the differential control of production pressure and reduce production damages during the extraction.

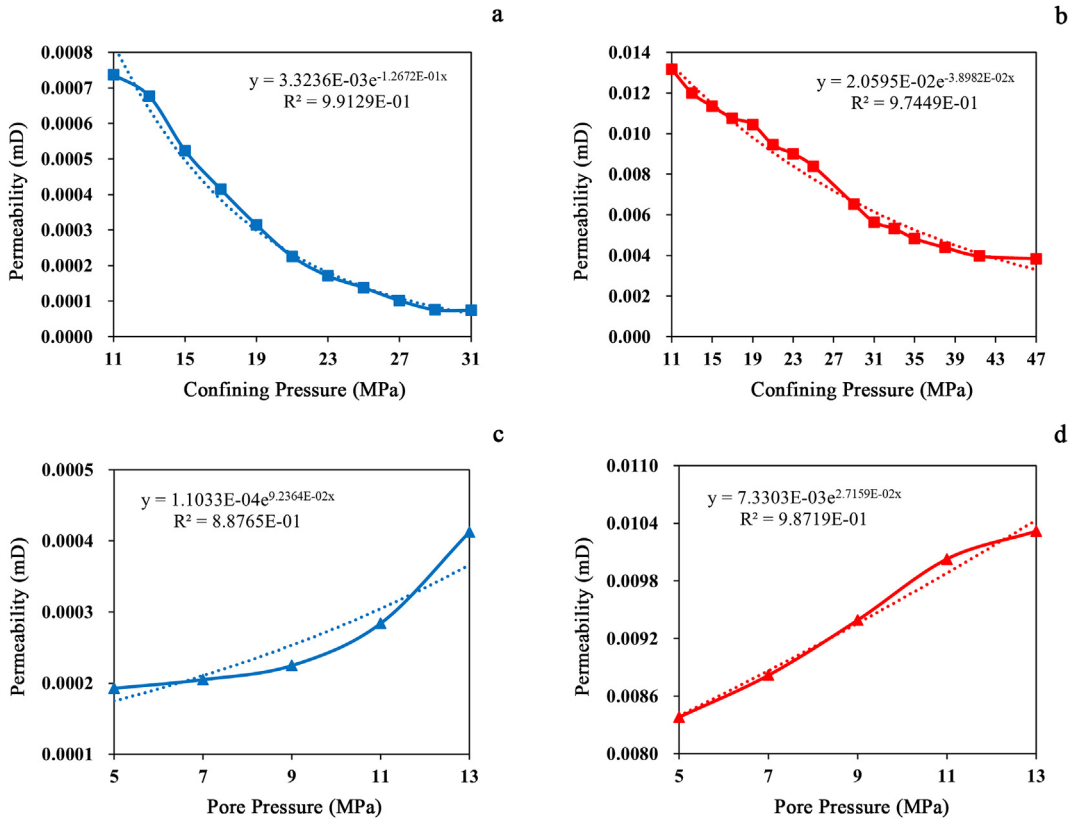

Fig. 15. Permeability versus confining pressure and pore pressure of (a, c) Longmaxi and (b, d) Wufeng Formations.

Declaration of competing interest

The authors declare that they have no known competing financial interests or personal relationships that could have appeared to influence the work reported in this paper.

Acknowledgments

The study was supported by the National Key R&D Program of China (Grant No. 2020YFA0711802) and the Strategic Program of Chinese Academy of Sciences (Grant No. XDB10030400). The authors would like to express their deepest gratitude for the generous support. In addition, the authors thank Dr. Zhongming Du, Dr. Jialong Liu, Dr. Jiao Su, and Ms. Yuxing Zhang from Institute of Geology and Geophysics, Chinese Academy of Sciences, for assistance in sample preparation, FIB-SEM imaging, and dataset processing.

List of symbols

K	Permeability
φ	Porosity
S	Matrix specific surface area
c	Kozeny–Carman constant
τ	Pore tortuosity
σ_{eff}	Effective stress
p_{c}	Confining pressure
p_{p}	Pore pressure
α	Biot coefficient

References

Chen, M.F., He, S., Yi, J.Z., 2019. Development characteristics of organic pore in shale gas reservoir of Wufeng Formation-Member 1 of Longmaxi Formation in Pingqiao block, Fuling shale gas field. Acta Pharmacol. Sin. 40 (4), 423–433.
Curtis, J.B., 2002. Fractured shale-gas systems. Am. Assoc. Petrol. Geol. Bull. 86 (11), 1921–1938.
Gale, J.F.W., Reed, R.M., Holder, J., 2007. Natural fractures in the Barnett Shale and their importance for hydraulic fracture treatments. Am. Assoc. Petrol. Geol. Bull. 91 (4), 603–622.
Goral, J., Andrew, M., Olson, T., Deo, M., 2020b. Correlative core-to pore-scale imaging of shales. Mar. Petrol. Geol. 111, 886–904.
Goral, J., Deo, M., Andrew, M., 2019b. Correlative Multiscale Imaging of Mancos Shale. International Petroleum Technology Conference, Beijing, China.
Goral, J., Panja, P., Deo, M., Andrew, M., Linden, S., Schwarz, J.O., Wiegmann, A., 2020a. Confinement effect on porosity and permeability of shales. Sci. Rep. 10 (1), 1–11.
Goral, J., Walton, I., Andrew, M., Deo, M., 2019a. Pore system characterization of organic-rich shales using nanoscale-resolution 3D imaging. Fuel 258, 116049.
Guo, T., 2013. Evaluation of highly thermally mature shale-gas reservoirs in complex structural parts of the Sichuan Basin. J. Earth Sci. 24 (6), 863–873.
Haghi, A.H., Chalaturnyk, R., Blunt, M.J., Hodder, K., Geiger, S., 2021. Poromechanical controls on spontaneous imbibition in earth materials. Sci. Rep. 11 (1), 1–11.
Haghi, A.H., Talman, S., Chalaturnyk, R., 2020. Consecutive experimental determination of stress-dependent fluid flow properties of Berea sandstone and implications for two-phase flow modeling. Water Resour. Res. 56 (1), e2018WR024245.
He, C., He, S., Guo, X., Yi, J., Wei, Z., Shu, Z., Peng, N., 2018. Structural differences in organic pores between shales of the Wufeng formation and of the Longmaxi Formation's first member, jiaoshiba block, Sichuan Basin. Oil Gas Geol. 39 (3), 472–484.
Huang, J.L., Ju, C.N., Li, J.Z., Dong, D.Z., Wang, S.J., Wang, S.Q., Wang, Y.M., Li, D.H., 2012. Shale gas accumulation conditions and favorable zones of Silurian Longmaxi Formation in south Sichuan Basin, China. J. China Coal Soc. 37 (5), 782–787.
Ji, L.L., Lin, M., Cao, G.H., Jiang, W.B., 2019a. A multiscale reconstructing method for shale based on SEM image and experiment data. J. Petrol. Sci. Eng. 179, 586–599.
Ji, L.L., Lin, M., Cao, G.H., Jiang, W.B., 2019b. A core-scale reconstructing method for shale. Sci. Rep. 9 (1), 1–12.
Ji, L.M., Zhang, T.W., Milliken, K.L., Qu, J.L., Zhang, X.L., 2012. Experimental investigation of main controls to methane adsorption in clay-rich rocks. Appl. Geochem. 27 (12), 2533–2545.

Ju, Y., Gong, W.B., Chang, C., Xie, H.P., Xie, L.Z., Liu, P., 2017. Three-dimensional characterisation of multi-scale structures of the Silurian Longmaxi shale using focused ion beam-scanning electron microscopy and reconstruction technology. J. Nat. Gas Sci. Eng. 46, 26–37.
Kang, J.W., Yan, J.F., Yu, Q., Tian, J.C., Men, Y.P., Sum, Y.Y., 2018. Characteristics of organic-rich shale in Wufeng–Longmaxi formations in Suiyang area of northern Guizhou and its implication to shale gas. Pet. Geol. Exp. 40 (2), 185–192.
Ke, K., 2015. Analysis of Shale Gas Geological Conditions of the Longmaxi Formation in the Southern Sichuan and Northern Guizhou. MSc Thesis. Chengdu University of Technology, Chengdu, China.
Latief, F.D.E., Fauzi, U., 2012. Kozeny–Carman and empirical formula for the permeability of computer rock models. Int. J. Rock Mech. Min. Sci. 50, 117–123.
Linden, S., Cheng, L., Wiegmann, A., 2018. Specialized Methods for Direct Numerical Simulations in Porous Media. Math2Market GmbH Technical Report.
Liu, Z.Y., Zhang, J.C., Liu, Y., Yu, W.W., Wei, H., Li, B.W., 2016. The particle size characteristics of pyrite in western Hunan and Hubei areas' Wufeng–Longmaxi Formation shale. Sci. Technol. Eng. 16 (26), 34–41.
Loucks, R.G., Reed, R.M., Ruppel, S.C., Hammes, U., 2012. Spectrum of pore types and networks in mudrocks and a descriptive classification for matrix-related mudrock pores. Am. Assoc. Petrol. Geol. Bull. 96 (6), 1071–1098.
Lüning, S., Craig, J., Loydell, D.K., Storch, P., Fitches, B., 2000. Lower Silurian 'hot shales' in North Africa and Arabia: regional distribution and depositional model. Earth Sci. Rev. 49 (1–4), 121–200.
Ma, L., Dowey, P.J., Rutter, E., Taylor, K.G., Lee, P.D., 2019. A novel upscaling procedure for characterising heterogeneous shale porosity from nanometer-to millimetre-scale in 3D. Energy J. 181, 1285–1297.
Mehmani, A., Prodanović, M., Javadpour, F., 2013. Multiscale, multiphysics network modeling of shale matrix gas flows. Transport Porous Media 99 (2), 377–390.
Qiao, L.P., Wang, Z.C., Li, S.C., 2011. Effective stress law for permeability of tight gas reservoir sandstone. Chin. J. Rock Mech. Eng. 30 (7), 1422–1427.
Saraji, S., Piri, M., 2015. The representative sample size in shale oil rocks and nano-scale characterization of transport properties. Int. J. Coal Geol. 146, 42–54.
Schieber, J., 2002. Sedimentary pyrite: a window into the microbial past. Geology 30 (6), 531–534.
Schieber, J., Baird, G., 2001. On the origin and significance of pyrite spheres in Devonian black shales of North America. J. Sediment. Res. 71 (1), 155–166.
Tahmasebi, P., Javadpour, F., Sahimi, M., Piri, M., 2016. Multiscale study for stochastic characterization of shale samples. Adv. Water Resour. 89, 91–103.
Wang, S.Y., 2013. The Study of the Shale (Gas) Features in Upper Ordovician–Lower Silurian, Uplift in the Northern of Guizhou. MSc Thesis. Chengdu University of Technology, Chengdu, Sichuan, China.
Wang, Y., Wang, L.H., Wang, J.Q., Jiang, Z., Wang, C.C., Fu, Y.N., Song, Y.F., Wang, Y.F., Liu, D.Z., Jin, C., 2019. Multiscale characterization of three-dimensional pore structures in a shale gas reservoir: a case study of the Longmaxi shale in Sichuan basin, China. J. Nat. Gas Sci. Eng. 66, 207–216.
Wilkin, R.T., Barnes, H.L., Brantley, S.L., 1996. The size distribution of framboidal pyrite in modern sediments: an indicator of redox conditions. Geochem. Cosmochim. Acta 60 (20), 3897–3912.
Xia, Y.D., Blumers, A., Li, Z., Luo, L.X., Tang, Y.H., Kane, J., Goral, J., Huang, H., Deo, M., Andrew, M., 2020. A GPU-accelerated package for simulation of flow in nanoporous source rocks with many-body dissipative particle dynamics. Comput. Phys. Commun. 247, 106874.
Xin, C., Chen, L., Guo, X.S., Wang, C., 2019. Geochemical characteristics of shale gas in the silurian Longmaxi Formation, jiaoshiba area, southeast Sichuan Basin, China. Energy Fuels 33 (9), 8045–8054.
Yan, J.F., 2017. The Shale Gas Accumulation Conditions and Distribution Characteristics of Black Shales in the Upper Ordovician Wufeng Formation–Lower Silurian Longmaxi Formation of Northern Guizhou. PhD Thesis. Chengdu University of Technology, Chengdu, China.
Yang, R., Hao, F., He, S., He, C.C., Guo, X.S., Yi, J.Z., Hu, H.Y., Zhang, H.W., Hu, Q.H., 2017. Experimental investigations on the geometry and connectivity of pore space in organic-rich Wufeng and Longmaxi shales. Mar. Petrol. Geol. 84, 225–242.
Zhang, H.X., Liu, W.Q., 2018. Seepage of marine-terrigenous facies coal measures shale. Chin. J. High Press. Phys. 32 (5), 157–164.
Zhang, Y.X., Ghanbarnezhad Moghanloo, R., Davudov, D., 2019. Pore Structure Characterization of a Shale Sample Using SEM Images. SPE Western Regional Meeting, San Jose, California, USA.
Zhou, M.H., Liang, Q.Y., 2006. Petroleum geological conditions of lower assemblage in Qianzhong uplift and peripheral regions. Mar. Orig. Pet. Geol. 11 (2), 17–24.
Zhou, S.W., Yan, G., Xue, H., Guo, W., Li, X.B., 2016a. 2D and 3D nanopore characterization of gas shale in Longmaxi formation based on FIB-SEM. Mar. Petrol. Geol. 73, 174–180.
Zhou, Y., Li, S.J., Zhang, R.Q., Ye, L.Q., Chai, T., 2016b. Characteristics of paleostructure and hydrocarbon accumulation of marine sequence in the Middle and Upper Yangtze region. J. Earth Sci. Environ. 38 (3), 365–377.

Xiaofang Jiang received her BSc degree from Wuhan University, China. In 2018, she started her PhD program in University of Chinese Academy of Sciences, Beijing, China and State Key Laboratory of Geomechanics and Geotechnical Engineering, Institute of Rock and Soil Mechanics, Chinese Academy of Sciences, Wuhan, China. Her PhD program focuses on pore structure characterization and multiscale flow in shale.